




Lithium-Ion Battery Life Model with Electrode Cracking and Early-Life Break-in Processes

Kandler Smith,^{1,z}  Paul Gasper,¹ Andrew M. Colclasure,¹ Yuta Shimonishi,² and Shuhei Yoshida²

¹National Renewable Energy Laboratory, Golden, Colorado, United States of America

²DENSO Corporation, Kariya, Aichi 448-866, Japan

This paper develops a physically justified reduced-order capacity fade model from accelerated calendar- and cycle-aging data for 32 lithium-ion (Li-ion) graphite/nickel-manganese-cobalt (NMC) cells. The large data set reveals temperature-, charge C-rate-, depth-of-discharge-, and state of charge (SOC)-dependent degradation patterns that would be unobserved in a smaller test matrix. Model structure is informed by incremental capacity analysis that shows loss of lithium inventory and cathode-material loss as the dominant capacity fade mechanisms. The model includes terms attributable to solid-electrolyte interface (SEI) growth, electrode cracking, cycling-driven acceleration of SEI growth, and “break-in” mechanisms that slightly decrease or increase available Li inventory early in life. The study explores what mathematical couplings of these mechanisms best describe calendar aging, cycle aging, and mixed calendar/cycle aging. Various approaches are discussed for extracting relevant stress factors from complex cycling profiles to predict lifetime during real-world battery loads using models trained on constant-current laboratory test results. The complexity of the present human-driven model identification process motivates future work in machine learning to more widely search and statistically discern the optimal model that correctly extrapolates capacity fade based on physical knowledge. © 2021 The Author(s). Published on behalf of The Electrochemical Society by IOP Publishing Limited. This is an open access article distributed under the terms of the Creative Commons Attribution Non-Commercial No Derivatives 4.0 License (CC BY-NC-ND, <http://creativecommons.org/licenses/by-nc-nd/4.0/>), which permits non-commercial reuse, distribution, and reproduction in any medium, provided the original work is not changed in any way and is properly cited. For permission for commercial reuse, please email: permissions@iopublishing.org. [DOI: [10.1149/1945-7111/ac2ebd](https://doi.org/10.1149/1945-7111/ac2ebd)]



Manuscript submitted April 7, 2021; revised manuscript received August 13, 2021. Published October 22, 2021.

Supplementary material for this article is available [online](#)

Accurate lifetime prediction is needed to bring maturity to large-scale battery applications such as electric vehicles (EV) and grid energy storage, with benefits for cell producers, system engineers, and end-users. Lifetime models help to establish warranty terms, replacement schedules, health-conscious controls, and create business models for battery first and second use. The ideal life model should accurately extrapolate degradation forward in calendar time and number of cycles after training on data from an accelerated aging test matrix. This model should furthermore interpolate (and possibly extrapolate) to untested aging conditions, as well as capture aging path-dependence for real-world mixed-use cases, (e.g., slow charging interspersed with occasional fast charging, periods of storage followed by cycling, and variable degradation with seasonal temperature changes).

Achieving these life-prediction goals is complicated by the multitude of nonlinear degradation mechanisms present in lithium-ion (Li-ion) batteries and the disparate ways they manifest themselves under accelerated and real-world aging. In this endeavor, two major open questions are: How is cycling degradation coupled to calendar degradation, and how does complex cycling damage, such as from an EV power profile, relate to simple constant-current (CC) cycle-aging conditions? Identifying solutions to these challenges is made more difficult by the inherent difference in variable battery usage in the real world, which may require 10- to 20-year lifetimes, compared to the limits of laboratory-based accelerated aging tests, which are often less than one year in duration and conducted under constant temperature and cycle aging conditions.

Multiple modeling approaches exist for life prediction. Neural-network and machine-learning models, reviewed by Hu et al.,¹ have limited extensibility beyond their training data to untested operating conditions. Further work is required to show their applicability not just for accelerated cycle aging, but for real-world mixed calendar/cycle-aging scenarios. Data-driven approaches have indeed proven effective in tracking health in an onboard control environment, using features derived from real-time current, voltage, and impedance measurements.²⁻⁷

At the opposite end of the spectrum from data-driven models, physics-based models describe and track individual mechanisms, as reviewed by Reiners et al.⁸ For the graphite anode, mechanisms include solid-electrolyte interface (SEI) growth^{9,10} and acceleration of SEI growth due to graphite microcracking¹¹ and transition metal dissolution/migration to the anode.^{12,13} Thick SEI can reduce electrode porosity, clogging pores and blocking Li diffusion in the electrolyte, potentially leading to the onset of Li plating.¹⁴ Li plating and SEI growth both contribute to loss of Li inventory (LLI) capacity fade. In addition to LLI, loss of active material (LAM) also impacts capacity fade. These two mechanisms can manifest in both parallel (additive) and competitive (minimum or maximum) manners. Predictive models of LAM range from semi-empirical current integration^{15,16} to mechanical stress/fatigue-coupled models.⁸ Physical models are valuable in that they bring understanding that can be used to optimize cell designs and operating conditions. Unfortunately, they are not automatically extensible to new cell designs without first ensuring that they mathematically describe all relevant degradation mechanisms for that new cell. They are also challenging to parameterize—requiring physical measurement and detailed electrochemical tests—as well as to compute in real-time controls.

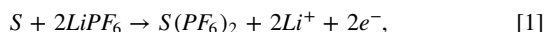
Reduced-order algebraic models¹⁷⁻²⁰ are a third class of life-predictive model, sitting somewhere between physics-based and data-driven approaches. Like physical models, they attempt to discern and track individual degradation mechanisms. Unlike physical models, they use ordinary rather than partial differential equations (respectively, ODEs vs PDEs). While most physics-based works pre-suppose a mathematical model, most life-prognostic works proceed backwards from the data, adding terms as needed—sometimes in an empirical fashion—to describe additional aging phenomena as they appear in the data. Additional terms to describe new aging phenomena can be physically supported through non-invasive cell characterization methods. Incremental capacity analysis is an invaluable diagnostic tool to quantify the contributions of LLI, anode LAM, and cathode LAM mechanisms to capacity fade.^{9,21} Within single aging conditions, LLI and LAM states can be extrapolated and have been shown to predict the onset of accelerated degradation, for example when anode LAM outpaces cathode LAM and LLI, which leads to Li plating.²²

^zE-mail: kandler.smith@nrel.gov

Reduced-order models often model calendar capacity fade as a function of time raised to some power, t^p , and cycling fade as a function of full-equivalent cycles raised to another power, N_{100}^z . For Li-ion batteries, a time exponent of $p \approx 0.5$ is most common^{9,18–20,23–34} attributed to diffusion-limited SEI growth. Under kinetic limitations, the exponent may approach $p \approx 1.0$.^{25–27} For a review of these and other reduced-order calendar aging models, see Table I of Gasper et al.¹⁷ Cycle aging models typically use an exponent near $z \approx 0.5$,^{19,35–39} interpreted as a surface process such as SEI microcracking or cathode transition metal dissolution/migration that accelerates SEI growth. Larger values, $0.6 < z < 0.9$ ^{40,41} or $z \approx 1$,²⁰ may be attributed to lithium lost when active sites are lost due to mechanical stresses of cycling. In the most common case where Li inventory limits relative capacity q , calendar and cycling mechanisms proceed in parallel and the effect of each mechanism may simply be added, $q_{Li} \sim q_0 -$ ^{18,20,37} The aging test matrix must vary time and cycling-throughput to adequately deconvolute their separate fade contributions.

Other mechanisms may combine competitively, rather than additively or multiplicatively. An example of this is the competition between the overall available Li in the cell (related to the LLI), overall capacity for Li storage in the cathode active materials (LAM_{PE}), and the overall capacity for lithium storage in the anode (LAM_{NE}). Active material availability is influenced by several different physical mechanisms. Cathode cracking is a well-documented mechanism for the present graphite/nickel-manganese-cobalt (NMC) cathode system with polycrystalline architecture. Cracking causes growth in secondary particle surface area due to separation of primary particle grain/grain boundaries,⁴² crystalline restructuring near the surface leading to slower kinetics,^{43,44} damage to transport paths including within the grain interior,⁴⁵ and electrical isolation.⁴⁶ Electrochemical-mechanical models predict that cracking saturates at the beginning of life and can be considered a break-in mechanism.⁴⁷ Actual data also show a continuous LAM with cycling, possibly due to continued crack growth due to fatigue, crystalline-restructuring-driven resistance growth, or electrical isolation within the composite electrode.⁴⁸

Less explored in lifetime models are “break-in” mechanisms that occur early in life, causing initial shifts in Li inventory and anode/cathode stoichiometry windows and thus capacity.^{20,49} When fitting a model, break-in magnitude can be estimated by throwing out data for the first tens of days or cycles and allowing the y-intercept, q_0 , to vary. Under mild cycling, NMC chemistries can show initial increases in capacity. This could be due to an initial drop in cell resistance with NMC surface growth, or due to electrolyte oxidation. Deshpande⁵⁰ proposed an electrolyte oxidation mechanism that may occur at fresh NMC surfaces where a solvent S reacts with $LiPF_6$ salt. The product Li intercalates into the cathode, improving the cell’s cyclable Li inventory,



and thus its initial capacity. Ideally, these reactions would occur during the formation process, however most formation protocols consist of low rate ($\sim C/10$), high temperature ($\sim 45^\circ C$) cycles. In contrast, the lifetime of the as-manufactured cell is typically spent cycling at higher rates and lower temperatures, both causing additional diffusion-induced stress and fresh surface area growth of the cathode. In addition to cycling-induced shifts, the time-

averaged state of charge (SOC) of the cell can also cause apparent shifts in Li inventory as Li slowly diffuses from the excess anode overhang area.^{19,51,52} The passive part of the anode can either reversibly increase or decrease the capacity depending on the SOC before the capacity measurement. If the pre-capacity-measurement SOC is higher than the mean-aging SOC, measured capacity can increase. Li may similarly slowly move in and out of partially isolated cathode and anode particles depending on dwell time at certain SOCs.

This paper develops a reduced-order capacity fade model for a dataset of 32 Li-ion graphite/NMC cells designed for EV application. The model incorporates lessons from the prior work to identify a physically justified model, while attempting to address key challenges for life-predictive models. The dataset and modeling analysis shed light on factors leading to electrode cracking, the coupling between calendar and cycle life, the presence of multiple break-in mechanisms and relationships between simple and complex cycling. We hope the work motivates future experiments and analyses to further improve life predictive accuracy and minimize the time and expense of aging experiments. In the following, the Experimental Section describes the aging test campaign. The Mathematical Model Section then introduces the reduced-order life model framework and references Appendices A-C that consider how to extrapolate the fitted model to complex aging scenarios. The Results Section identifies degradation mechanisms from the data and develops the capacity model for the present graphite/NMC cell.

Experimental

Aging tests were conducted on 32 Li-ion prismatic cells of 50-Ah class capacity with graphite anode and $Li-Ni_{0.6}Mn_{0.2}Co_{0.2}O_2$ cathode and total mass of 860 g. The prismatic hard-can cells follow the PHEV2 form factor (length: 148 mm, height: 91 mm, thickness: 26.5 mm) from the VDA (German Association of the Automotive Industry). Maximum charge and discharge rates are 1C and 3C, respectively. Table I summarizes calendar aging tests performed on 11 cells at various temperatures and SOCs. Table II summarizes cycle aging tests performed on 19 cells at various temperatures, charge C-rates, and min/max SOC windows. Throughout this paper, depth-of-discharge is defined as $DOD = SOC_{max} - SOC_{min}$. All aging cycles used CC cycling protocols, with 10-minute rests at the end of charge and discharge, except for a 50% duty-cycle cell which had additional rest time—spent equally at the end of charge and end of discharge—such that approximately half its life was spent cycling and half its life was spent at rest. The 50% duty-cycle cell is used to validate the model’s coupling between calendar and cycle life. Two additional cells were aged under a world-harmonized test protocol (WLTP) EV drive cycle at 25 °C between 5%–90% ΔSOC with C/3 constant-current constant-voltage (CCCV) charging to 4.11 V with a 0.5A cutoff and 10-minute rests following charge and discharge. The WLTP drive cycle cells are used to validate how well the life model fit to simple cycling test conditions extends to complex cycling. FUJITSU TNW 5V,360A cyclers controlled electrical charge/discharge; ESPEC CORP. BT2–408C environmental chamber controlled the cell ambient temperature environment. In fitting the model, the average measured cell temperature is used, rather than ambient temperature. Cell temperature was measured at the middle-top surface of the cell.

Each aging test was interrupted for a reference performance test (RPT) approximately once per month for calendar-aging cells and once per 100 cycles for cycle-aging cells. Performed at 25 °C, the nominal RPT consisted of a C/3 partial discharge to 2.75V, 30-minute rest, a CCCV charge at C/3 rate to 4.25V with C/100 cutoff, 10-minute rest, followed by a C/3 discharge to 2.75V. Every second RPT, a supplemental C/20 full charge and discharge was run with the same voltage and current cutoff limits and 10-minute rest period. The C/20 cycling data are used for incremental capacity analysis which fits open-circuit potential curves for the anode and

Table I. Calendar-aging conditions.

SOC/T	10 °C	25 °C	45 °C	55 °C	60 °C
10%			X		
50%		X	X		
90%	X	X	X	X	X
100%		X	X	X	

Table II. Cycle-aging conditions, listing charge C-rate. Discharge C-rate is 1C for all cases.

$\Delta SOC/T$	10 °C	25 °C	45 °C	55 °C	60 °C
40%–60% (20% DOD)			0.33		
10%–50% (40% DOD)		0.33	0.33		
30%–70% (40% DOD)			0.33		
50%–90% (40% DOD)		0.33	0.33		
20%–80% (60% DOD)			0.33		
30%–90% (60% DOD)			0.33		
10%–90% (80% DOD)	0.33	0.33	0.33	0.33	0.33
		1	1	1	
			0.33 (50% duty cycle)		
20%–100% (80% DOD)			0.33		
0%–100% (100% DOD)			0.33		

cathode to full-cell data. To support the analysis, one 50-Ah class cell was disassembled, coin half cells were constructed and cycled at the C/100 rate to measure the anode and cathode's open-circuit potential vs metallic Li.

Mathematical Model

We generalize a reduced-order life model framework²⁰ and summarize how to convert the fitted model (valid for simple cycling) to time-series form (valid for complex cycling)⁵³ with further details given in Appendices. The model is identified by fitting degradation mechanism trial equations to accelerated aging data. Degradation mechanism and rate equations are selected that statistically best represent the data and can be physically justified, for example with incremental capacity analysis.

Degradation mechanism models.—Changes in a battery performance metric, y , are represented as a mathematical combination of degradation mechanism state equations x_i shown in Table III. In simple cases where a single degradation mechanism dominates (e.g. LLI in the present work), a linear combination of state equations often suffices,

$$y = \sum_i x_i. \quad [2]$$

Performance metrics, y include battery relative resistance, r and relative capacity, q . In more complex cases, multiple mechanisms may control battery capacity fade and the dominant mechanism may change during lifetime. An example²⁰ is

$$q = \min(q_{Li}, q_-, q_+), \quad [3]$$

where separate submodels represent anode inventory, $y_- = q_-$, cathode inventory, $y_+ = q_+$, and lithium inventory, $y_{Li} = q_{Li}$. This multi-mechanism model can mimic some types of sudden-death or “rollover” behavior. Rollover is not evident in the present dataset or considered in this work however.

In Table III, x is the state variable for degradation mechanism i , p is the order of the fade mechanism (a constant in this work), k is the rate of fade, and M is the magnitude of fade. Table III provides degradation models in both ordinary-differential (valid for variable fade rate) and time-integrated analytic-solution form (valid for constant fade rate). Accelerated aging tests are generally conducted at constant values of temperature T , depth of discharge DOD , average state of charge SOC , and discharge/charge C-rates, $C_{rate} = I/Ah_0$, where I is current and Ah_0 is cell nameplate capacity. For individual aging tests under simple aging, k is constant and the time-integrated analytical solution is used to select the mechanism and fit its rate k . After k is determined for multiple aging conditions,

a rate-law function is developed to describe rate as a function of aging condition, e.g. $k(T, SOC, DOD, C_{rate})$.

Rate-law sub-models.—Table IV lists acceleration factors, θ_h , commonly used in the literature in rate-law sub-models. These sub-models are generally built as multiplicative combinations of acceleration factors,

$$k_i = k_{i,ref} \prod_h \theta_h, \quad [4]$$

though in the case of multiple mechanisms, j , additive terms are also possible,

$$k_i = \sum_j k_{ij,ref} \prod_h \theta_{hj}. \quad [5]$$

Extension from simple to complex cycling.—Several accommodations are made to transform the model fitted to CC cycling with static-aging conditions to a time-series form capable of handling complex-cycling dynamic-aging conditions for arbitrary $T(t)$, $SOC(t)$ and $C_{rate}(t)$. Each state equation (Table III) is integrated for varying rate \bar{k} where the overbar indicates a “normalized” version of fade rate k . The norm of the fade rate allows for (1) time-scale separation and (2) calculation of cycling damage accrued by complex cycling. Normalization can be thought of as converting the complex cycling damage that occurs at a fast time scale to an average value that can be integrated at a slower time-scale.

Timescale-separation.—For cases where the electrochemical simulation of short-term cycling behavior is computationally intensive, timescale separation relaxes the need to simulate thousands of cycles to predict lifetime. Using the forward Euler method,⁵⁶ only a handful of representative cycles need be simulated to represent changes throughout lifetime.⁵⁷ For time-varying states, $x(t)$, the normalized fade rate \bar{k} is simply the time average of the variable fade rate $k(t)$

$$\bar{k}_i = \frac{1}{\Delta t} \int_0^{\Delta t} k_i(t) dt. \quad [6]$$

Cumulative damage accrued by complex cycling.—Cycle-varying states, $x(N)$, cannot be continuously integrated over time. For any life-prognostic model in which number of cycles, N , is an independent variable, the user must make either make the restrictive assumption that cycles are accumulated proportional to instantaneous current or come up with some method to count cycles accrued over a given time-period. These two normalization methods are current integration and Rainflow cycle counting⁵⁸ and are further

Table III. Degradation mechanism models.

Mechanism	State equation	Analytical solution	Conversion from cycle- to time-based degradation rate
1) Mixed diffusion/kinetic-limited side reaction ^{a,b)}	<ul style="list-style-type: none"> Valid for complex aging (variable k) Solved via time integration $\dot{x}(t) = \bar{k}_t p \left(\frac{\bar{k}_t}{x} \right)^{\frac{1-p}{p}}$	<ul style="list-style-type: none"> Valid only for simple aging (constant k) Used for model identification $x(t) = k_t t^p$	$\bar{k}_t = \left(\frac{\bar{k}_N}{\Delta t} \right)^p$
2) Site loss ^{c)}	$\dot{x}(t) = \bar{k}_t \left(\frac{x_0}{x} \right)^p$	$x(N) = k_N N^p$ $x(t) = x_0 - [x_0^{1+p} - k_t x_0^p (1+p)t]^{\frac{1}{1+p}}$	$\bar{k}_t = \left(\frac{\bar{k}_N}{\Delta t} \right)$
3) Break-in process ^{d,b)}	$\dot{x}(t) = \bar{k}_t (\max[0, M - x(t)])$	$x(N) = x_0 - [x_0^{1+p} - k_N x_0^p (1+p)N]^{\frac{1}{1+p}}$ $x(t) = M(1 - \exp(-k_t t))$ $x(N) = M(1 - \exp(-k_N N))$	$\bar{k}_t = \left(\frac{\bar{k}_N}{\Delta t} \right)$

a) Order $p = 0.5$ for diffusion-limited SEI growth, $p = 1.0$ for kinetic-limited and $0.5 < p < 1.0$ for mixed cases. Typical m-norm value (see Section 3.3.2), $m = \infty$ relates mechanical damage to SEI surface. b) Appendix A provides numerical considerations for integration. c) Order $p = 0$ for linear fade. $p \geq 1$ for accelerating fade. At $p = 1$, the rate of site loss is inversely proportional to the amount of remaining electrode sites. An m-norm value, $m = 1$ sums the cumulative damage of individual microcycles (Miner's rule⁵⁴). Root sum of squares, $m = 2$, or maximum damage, $m = \infty$, may also be used. d) Typical m-norm value, $m = \infty$, accounts for damage due to break-in processes.

Table IV. Acceleration factors used for building degradation rate laws.

Rate/magnitude dependence	Type of Stress	Acceleration factor, θ_h^{a-d}
Temperature	Chemical & Mechanical	(1.1) $Arr_{E_a} = \exp\left[-\frac{E_a}{R_{ug}}\left(\frac{1}{T(t)} - \frac{1}{T_{ref}}\right)\right]$
SOC	Chemical	(2.1) $\exp\left[\frac{\alpha F}{R_{ug}} \frac{\eta(t)}{T(t)}\right]$ where $\eta(t) = U_{\pm}(t) - U_{ref}$
C-rate	Chemical	(2.2) ... where $\eta(t) = U_{\pm}(t) - U_{ref} - C_{rate}(t)R_{film}$
DOD	Mechanical	(3.1) $C_{rate,i}\sqrt{I_{pulse,i}} = \sqrt{DOD_i}\sqrt{C_{rate,i}}$ ⁵⁵
	Mechanical	(4.1) $(DOD_i)^\beta$
	Mechanical	(4.2) $(1 + \gamma(DOD_i)^\beta)$ (4.3) $\exp(\gamma(DOD_i)^\beta)$

a) i is cycle index from Rainflow algorithm. b) Fitting parameters are k_{ref} , E_a , α , R_{film} , γ , β . c) Constants are $R_{ug} = 8.314 \text{ J K}^{-1} \text{ mol}^{-1}$, $F = 96485 \text{ C mol}^{-1}$, and arbitrary user choice of T_{ref} and U_{ref} , with units of [K] and [V], respectively. d) U_- and U_+ , respectively negative and positive electrode equilibrium potentials, are functions of SOC.

described in Appendix B. Appendix C introduces a convolution formula as an alternative to Rainflow cycle counting. It allows integration of current with respect to fractional powers of time.

For rates that are functions of Rainflow microcycles $i = 1$ to n , the modified m-norm calculates a normalized degradation rate valid over the aging period Δt

$$\bar{k}_N = \|k_N\|_m = \left(\sum_{i=1}^n N_i |k_{N,i}|^m\right)^{1/m}. \quad [7]$$

With $m = 1, 2 \dots \infty$, the m-norm is similar to respective $L_1, L_2 \dots L_\infty$ norms, but with accommodation to account for whole or half cycles, $N_i = 1.0$ or 0.5 . With $m = \infty$, $\bar{k}_N = \|k_N\|_\infty = \max |k_{N,i}|$ selects the part of the cycle that causes the maximum damage. With $m = 1$, the norm sums the damage of all microcycles, equivalent to Miner's Rule.⁵⁴

The present time-series model integrates all state equations with respect to time (Table III, column 2). Cycle-based fade, \bar{k}_N , is converted to time-based fade, \bar{k}_t , using the chain rule (Table III, column 4).

Results

Figure 1 shows capacity fade for the 11 calendar aging tests, 19 simple-cycling aging tests, and 2 complex-cycling aging tests carried out over 200–300 d on the 50-Ah-class prismatic graphite/NMC cell. Here, we develop a physically relevant reduced-order life model describing C/3 capacity fade and highlight observed degradation mechanisms. Incremental capacity analysis, conducted on C/20 capacity fade data, is first used to diagnose the main capacity fade mechanisms. Compared to C/20, the C/3 data has 0.7 to 1.0 Ah less capacity at beginning of life (Fig. 2). This C/20 vs C/3 capacity difference reduces slightly in some cases but mostly stays constant throughout life, ranging from 0.5 to 1.0 Ah at end of test. An exception is the 45 °C 100% DOD cell #30 which has 2.3-Ah less capacity at C/3 vs C/20 at end of test. Compared to other cells with –5% to 25% 10-second direct-current (DC) resistance growth during the aging campaign, the 45 °C 100% DOD cell experienced 50% resistance growth, contributing to its additional capacity fade. It is our hope that degradation mechanisms observed here will motivate enhancement of physics-based models that directly capture the interplay of resistance growth and capacity fade across multiple rates other than the single C/3 rate considered here. This might be accomplished by introducing physical or empirical fade-rate equations for health-relevant parameters of a pseudo-2D electrochemical model. Data from all figures are published in the Supplemental Information (available online at stacks.iop.org/JES/168/100530/mmedia) accompanying this paper.

Incremental capacity analysis.—Illustrated in Fig. 3a, incremental capacity or dQ-dV⁻¹ analysis quantifies the impact of individual thermodynamic mechanisms—LAM_{NE}, LAM_{PE}, and LLI—in controlling C/20 capacity fade. Following the work of Dubarry,²¹ three variables were fit to C/20 data: positive electrode capacity, QPE , negative electrode capacity, QNE , and the offset, OFS , between the fully lithiated cathode and fully delithiated anode, either of which can limit discharge capacity. Based on these fitted variables, we observe a strong correlation (Fig. 3b) between C/20 capacity loss and LLI, expressed as

$$LLI = (QPE_{initial} - QPE_{deg}) - (OFS_{initial} - OFS_{deg}). \quad [8]$$

Typical for Li-ion cells, this correlation suggests that Li inventory controls capacity for the present 50-Ah class cell and dataset. But even though this correlation is good, the LLI is consistently lower than the actual capacity loss, indicating the need to include additional loss mechanisms to fully account for the lost capacity. These observations support the hypothesis that capacity loss can be modeled as the sum of Li loss due to Li-consuming side reactions (time-dependent, with uncertain coupling to cycling condition) and positive electrode loss (cycling dependent).

Model identification.—The capacity fade model identified here captures C/3 capacity as a function of time, cycles, temperature, DOD, charge C-rate, and SOC. Unlike typical model identification or parameter optimization problems, the equations that describe capacity fade across all test conditions are not known *a priori*. A hierarchical procedure is used to identify both equations and parameters:

- 1) *Local model*—Identify mechanisms (trial equations from Table III) that best match data and have physical justification. Identify the rate of fade, k , for each separate aging condition.
- 2) *Rate model*—Visualize how fade rate, k , depends on stress factors T , SOC , DOD , C_{rate} , etc. Select acceleration factor models (Table IV) that describe the rate of fade across multiple aging conditions.
- 3) *Global model*—Substitute rate models into local model equations. Refit selected model parameters to all datasets simultaneously.

Custom-developed Matlab[®] code partly automates the process, with functions to visualize and perform calculations on the data, filter and down-select subsets of data, build model equations, perform parameter fitting (function `nlinfit`), visualize fitted model results and evaluate quality-of-fit statistics (R-squared, adjusted R-squared, root-mean-square error). A shortcoming of the present

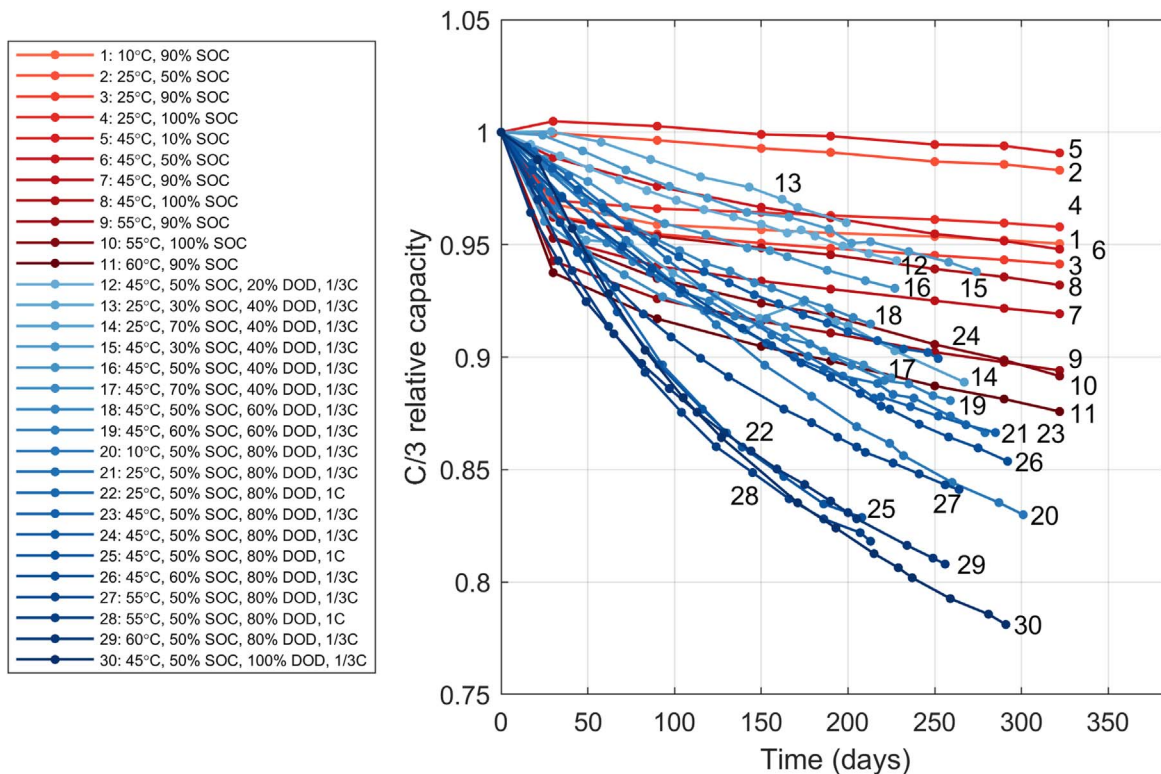


Figure 1. C/3 capacity vs time.

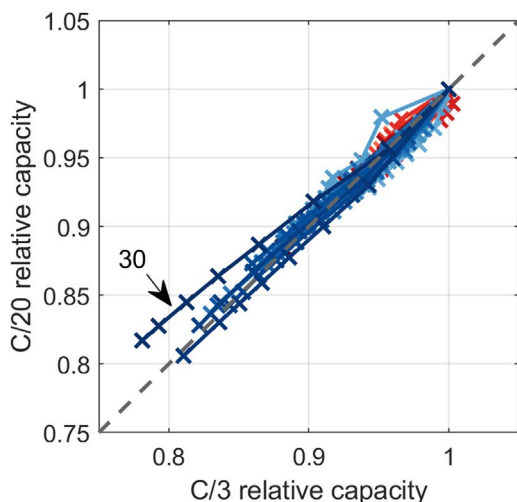


Figure 2. Correlation between C/20 and C/3 relative capacity.

work, however, is that model selection requires significant expert judgement and human labor. Future work will include machine learning concepts including multi-level optimization, symbolic regression, penalized regression, cross validation, and uncertainty quantification to automate the model development process and reduce human bias. Our recent work, for example, applied machine learning to identify a calendar fade model for an iron-phosphate/graphite Li-ion battery.¹⁷ Several restrictions on that method’s allowed equation formats must be relaxed to capture cycle aging for the present dataset.

Based on incremental capacity analysis, we hypothesize that relative capacity can be modeled as the sum of LLI due to calendar fade and cycling fade, together with a break-in mechanism that captures an initial shift in capacity early in life,

$$q = 1 - b_1 t^p - b_2 N^z - b_3 [1 - \exp(-t/\tau)] \quad [9]$$

To help determine the exponent p , Fig. 4a shows a log-log plot of C/3 capacity fade vs time. Reference lines show example square-root-of-time and linear-with-time trends. Figure 4b shows C/20 capacity fade vs time. Focusing first on the C/3 rate (Fig. 4a), most aging cases appear to eventually converge to square-root-of-time behavior, $p = 0.5$, albeit from different directions and with a long convergence time, 100 to 200 d. Calendar- and cycle-aging conditions converge towards $p = 0.5$ with a different slope. Calendar aging cases have a shallow slope that indicates negligible initial fade and/or offsetting mechanisms. An example offsetting mechanism is long-term SEI-growth-induced Li loss that is initially compensated by a short-term break-in mechanism that increases Li capacity. The C/3 data also shows that several cycling conditions with negligible calendar fade, specifically combinations of low temperature and low SOC, may have an exponent as high as $p = 1.0$. However, with just 1%–2% fade after 300 d, this is within the measurement noise. Despite clear trends across the data set, the variation of the exponent p vs both time and testing conditions is quite substantial, so it is difficult to assign a single value to p from the C/3 data.

Fortunately, the C/20 data (Fig. 4b) show a clearer picture, with less influence of break-in mechanisms. Here, most cycling conditions converge in around 100 d to $p = 0.5$. Although there are only three C/20 fade datapoints, there is very little noise in the data, and all calendar aging conditions show a consistent slope close to $p = 0.5$. To keep RPT capacity checks short, most aging campaigns conduct the “normal” RPT capacity check at the device-relevant rate (here, C/3). Less frequently, “supplemental” RPTs measure capacity at a slow rate (here, C/20) for incremental capacity analysis. Since C/20 data converge faster to a long-term trend and are more informative (Fig. 4), we suggest that in the future, a quick pseudo-low-rate capacity measurement be included as part of each normal RPT capacity check. A fast way to estimate C/20 capacity is to run a cascade discharge, whereby the normal C/3 discharge is followed by

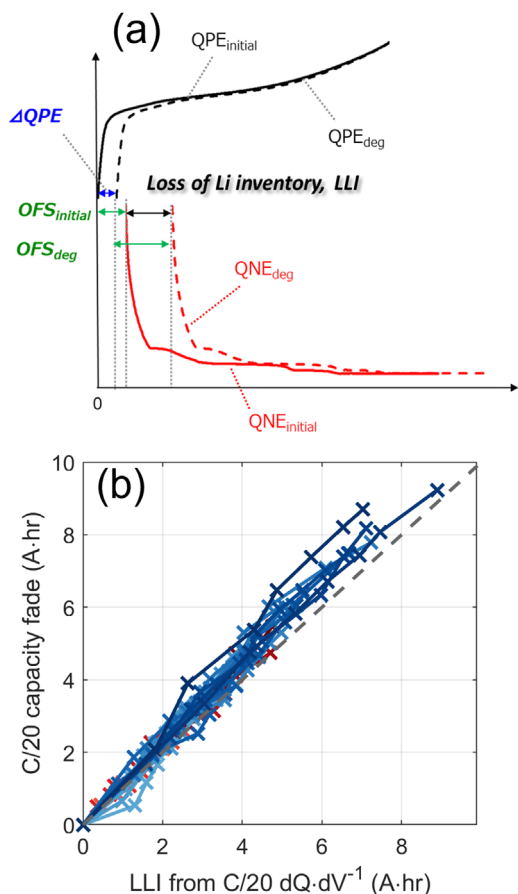


Figure 3. (a) Schematic showing relationship between LLI and fitted dQ/dV variables QPE, QNE, and OFS for cells in their initial and degraded states. (b) LLI closely correlates with C/20 capacity fade for all cells throughout aging.

additional discharge steps at progressively lower rates down to C/20, each proceeding to the cutoff voltage. The pseudo-C/20 capacity would be taken as the sum of capacity removed at all rates, from C/3 down to C/20. In this manner, C/20 capacity could be estimated with minimal additional test time.

The C/20 data do not support the use of a variable exponent calendar aging model. Early-life deviations from a constant exponent can be handled with break-in mechanisms. The constant exponent $p = 0.5$ suggests diffusion-limited SEI growth is the dominant long-term calendar-aging mechanism. To fit calendar-aging, we simplify the overall model (Eq. 9) by eliminating the cycling term $b_2 N^z$ and retaining only the steady-state of break-in magnitude b_3 ,

$$q = 1 - b_1 t^{1/2} - b_3 \quad [10]$$

Parameters b_1 and b_3 are fit to calendar aging data at long times, $t > 100$ d. Figure 5a shows the results of this local-model fit.

Figure 5b shows calendar fade rates, $b_1(T, SOC)$, for the calendar aging conditions. For graphite negative electrodes, fade rate typically increases monotonically with SOC and is described with a Tafel equation (Table IV, Eq. 2.1) whose functional dependence on negative electrode equilibrium potential results in a monotonic rate increase with SOC. At 25 °C however, data show the fade rate is non-monotonic, increasing slightly from 50% to 90% SOC, but then decreasing from 90% to 100% SOC. At 45 °C, fade is almost identical at 90% and 100% though both are much less than 50% SOC. And at 55 °C, fade is greater at 100% than 90%. Given the plethora of literature on graphite SEI growth, graphite SEI is

doubtless a prominent Li-loss fade mechanism here. It is likely some secondary cathode reaction is present. Regarding apparent capacity increase, Deshpande⁵⁰ proposed an electrolyte oxidation mechanism at high SOC where LiPF₆ salt reacts and Li intercalates into the cathode, supplementing the cell's cyclable Li inventory. Rodrigues et al. discuss solvent oxidation occurring at high cathode potentials resulting in increased Li inventory from charge neutrality and capacity gain for lithium titanate (LTO) cells during storage.⁵⁹ Regarding capacity decrease, manganese dissolution is another possible secondary reaction, where Mn dissolves from the NMC cathode and migrates to the graphite anode, accelerating graphite SEI growth.⁴⁴ We were unable to find any physically reasonable two-reaction Tafel model that could fully describe the dataset. Instead, we fit an empirical polynomial in SOC, multiplied by an Arrhenius temperature dependence shown in Table V, rate model (A). The formulas and activation energy, $E_a = 36,000 \text{ J mol}^{-1}$ are consistent with graphite SEI growth.⁶⁰ To keep notation compact, Table V abbreviates the Arrhenius formula as:

$$Arr_{E_a} = \exp \left[-\frac{E_a}{R_{ug}} \left(\frac{1}{T(t)} - \frac{1}{T_{ref}} \right) \right]$$

where the subscript E_a corresponds to the activation energy of the modeled reaction. Also regarding notation, subsequent cycling models (B) through (D) in Tables V and VI reference calendar fade rate model (A) as $(b_{1,t})_A$. This calendar fade model is later slightly improved to improve the overall fit to cycle aging data which include several additional levels of average SOC's. In the following discussion, subsequent improvement in local, rate, and/or global models is denoted in alphabetical order, labeled (A) through (F).

To model cycling fade, we must first estimate the exponent z in the cycling term $b_2 N^z$. Figure 4c isolates “pure capacity fade” by subtracting off fade due to calendar aging and break-in mechanisms. Most aging conditions at 45 °C and above rapidly converge to square-root-of-full-equivalent cycles, $N_{100}^{1/2}$. One exception is 45 °C 100% DOD, which initially displays a superlinear trend before converging to $N_{100}^{1/2}$ beyond 1000 cycles. For all cells cycling at 25 °C and below, pure cycling fade is initially superlinear, $z > 1.0$, up to around 400 cycles and then transitions to linear, $z \approx 1.0$, from cycles 400 to 900. Beyond 900 cycles, low temperature C/3 data are inconclusive whether the final exponent is $z = 0.5$. Compared to C/3 data, the C/20 data (Fig. 4d) provides insight. The C/20 data more quickly and uniformly converge to $z = 0.5$. It remains an open question whether some low-temperature cycling conditions will eventually reach $z = 0.5$ beyond 1000 cycles. But given the long-term convergence behavior shown for cases with a higher number of accumulated cycles, we assume $z = 0.5$ for the entire dataset. The exponent indicates this cycling-driven mechanism is likely coupled to a diffusion-limited process. Possibilities include SEI microcracking, Mn dissolution from the cathode with precipitation on the anode accelerating SEI growth, cathode cracking and grain isolation from diffusion-induced stress and/or cathode surface reconstruction.

Given that all aging conditions accumulate charge/discharge cycles proportional to time, $N \sim t$, so far it is not possible to tell whether the b_1 term is solely attributable to calendar fade, $t^{1/2}$, with some acceleration factor to account for, e.g., micro-cracking of the graphite surface; or if it also depends on square-root of cycles, $N^{1/2}$, for cycle aging tests. We thus test three different hypotheses. Table V compares three SEI local/rate model combinations—(B), (C), and (D)—that couple calendar-dependent SEI growth, $b_{1,t}$, with cycling-driven SEI damage, $b_{1,N}$, in different ways:

(B) Multiplicative: $b_{1,t} b_{1,N} t^{1/2}$

(C) Additive, proportional to partial-cycle count: $b_{1,t} t^{1/2} + b_{1,N} N^{1/2}$

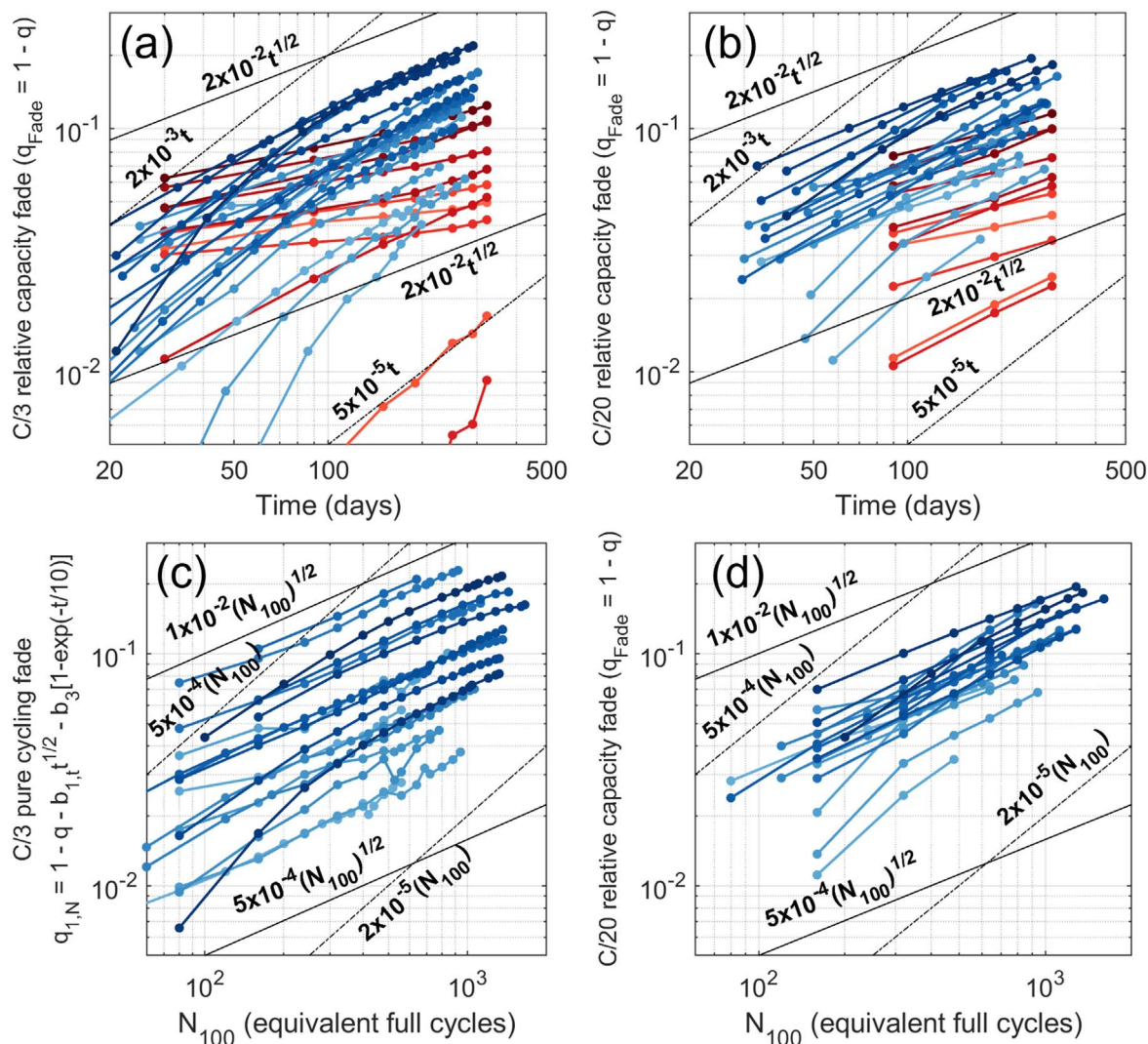


Figure 4. Log-log plots of (a) C/3 capacity fade vs time, (b) C/20 capacity fade vs time, (c) C/3 pure cycling fade vs cycles, and (d) C/20 capacity fade vs cycles. Trendlines show Linear and square-root behavior with each x -axis variable. In (c), pure cycling fade subtracts the model-estimated calendar fade from capacity-fade data.

(D) Additive, proportional to equivalent-full-cycle count: $b_{1,t} t^{1/2} + b_{1,N} N_{100}^{1/2}$

All three cycling-driven fade-rate models use the same functional form,

$$b_{1,N} = \max[0, b_{1,N,ref1} Arr_{E_{a1}} (DOD^{0.5} C_{chg}^{0.5}) (1 + a SOC) - b] + b_{1,N,ref2} Arr_{E_{a2}} DOD^c \quad [11]$$

with fitted parameters $b_{1,N,ref1}$, E_{a1} , a , b , $b_{1,N,ref2}$, E_{a2} , and c . While not exclusive, this chosen function matches well with trends observed in the rate data when interpreted with the three different local models, (B) through (D):

- At a fixed temperature and SOC, rate $b_{1,N}$ is nearly linear with $C_{chg} \sqrt{t_{chg}} = DOD^{0.5} C_{chg}^{0.5}$. This stress factor serves as a proxy for Li concentration gradient severity within an active material particle⁵⁵ which correlates with diffusion-induced stress.⁸ To aid visualization, Figs. 6a and 6b plot $b_{1,N}$ on log and linear scales, respectively.

- Plotted vs $DOD^{0.5} C_{chg}^{0.5}$, a straight line fit to rate $b_{1,N}$ does not pass directly through the origin (Fig. 6b). A slight offset, b , is

required, which can be interpreted as a threshold below which diffusion-induced stress does not cause damage.

- At 40% DOD, for which the dataset includes several different average SOC, we note that fade rate increases with SOC which, lacking more data, we capture as a linear function of SOC, with $a \sim 2$. Indeed, nano-indentation measurements show NMC₅₃₂ elastic modulus, hardness and interfacial fracture toughness all decrease with increasing SOC,⁶¹ by factors of 1.3, 1.2 and 1.8, respectively from 0% to 100% SOC.

- Temperature dependence follows the Arrhenius formula with activation energies ~ -30 to -50 kJ mol⁻¹ having negative values due to increased transport limitations (e.g., 45 kJ mol⁻¹ for NMC⁶²), diffusion-induced stress and material embrittlement at lower temperatures.

- Finally, the single 100% DOD test case at 45 °C could not be fit without including a power-law term, DOD^c , with a value of $c \sim 6$. This term slightly improves the overall fit and can be interpreted as a strain-induced particle damage that is independent of rate. Recall that this 100% DOD case experienced substantially more resistance growth than all other cells.

While the R^2 of models (B) through (D) are similar, two other metrics support the selection of model (D). As a test for how well the model extrapolates accelerated cycling (100% duty cycle) to real-

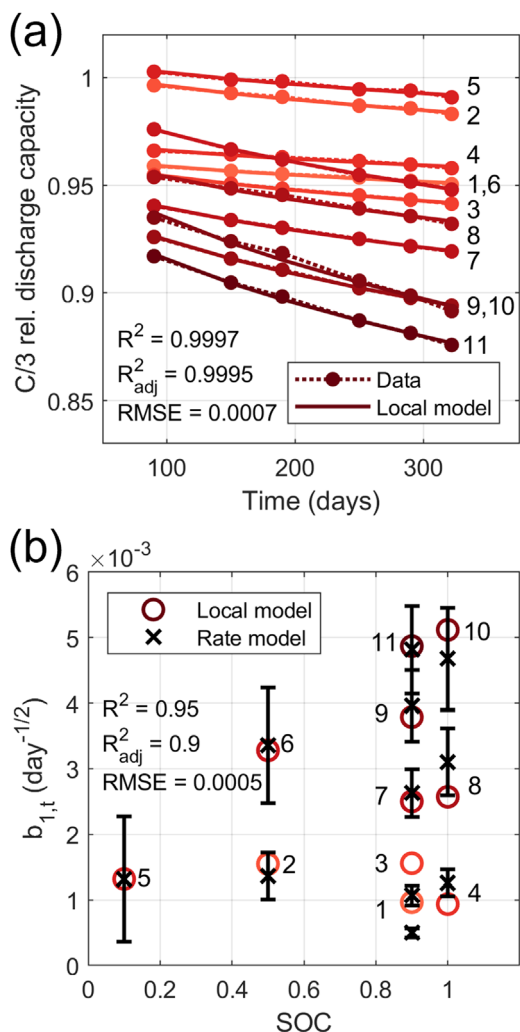


Figure 5. (a) Local model “(A)” in Table V, with two separate parameters, b_1 and b_3 , individually fit to each of the 30 aging test conditions. (b) Rate model “(A)” in Table V describing calendar fade rate vs T and SOC for the 10 storage aging test conditions.

world cycling, where there is rest between each charge/discharge cycle, the aging test matrix included one 50% duty-cycle case at 45 °C and 80% DOD. This 50% duty-cycle cell cycled half of each day and rested the other half of the day, with rest evenly distributed at end of discharge and end of charge. For the model to be consistent, the cycling fade rate $b_{1,N}$ should be the same for both the 50% and 100% duty cycles. Table VI shows this is exactly the case for additive models (C) and (D) with $b_{1,N}$ differing less than 0.6% between the 50% and 100% duty-cycle cells. In contrast, the multiplicative model (B) has 16% difference between the 50% and 100% duty-cycle cells. While further validation is still desired, this provides strong evidence that calendar-driven SEI growth is additive with cycling-driven damage.

Models (C) and (D) track cycling damage differently, vs partial cycles N and full-equivalent cycles M_{100} , respectively. Table V shows RMSE decreases 27-fold when using full equivalent cycles (D) compared to partial cycles (C). Full-equivalent cycles is also a more convenient metric to extrapolate the model from simple to complex cycling; the cycle-counting algorithm, (e.g., Rainflow, is not needed to count partial cycles).

With the SEI-growth models identified, we move to fitting the break-in mechanisms’ steady-state magnitude, b_3 . This parameter captures the y-intercept offset in capacity beyond the first tens of

days. Since capacity is Li-inventory limited, this equates to a loss or gain of Li, or similarly, a degradation or improvement of particle-scale Li transport that saturates early in life. Figure 7 plots break-in magnitude for the 30 test conditions fit using local model (E) in Table VII. Two trends are apparent:

- 1) For calendar-aged cells, b_3 follows a non-monotonic trend where it is negative at low SOC— an apparent Li-inventory gain, and positive at high SOC indicating a Li-inventory loss (Fig. 7a).
- 2) For cycled-aged cells, b_3 generally decreases— indicating a Li-inventory gain— monotonically with the diffusion-induced stress acceleration factor, $DOD^{0.5}C_{chg}^{0.5}$. Temperature also plays a role (Fig. 7b).

For the calendar-aged cells, model (E) in Table VII for $b_{3,t}$ captures the SOC-dependent trend. Usable Li-inventory gain increases from 10% to 30% SOC, decreases from 30% to 90%, then slightly increases again from 90% to 100% SOC. As mentioned in the introduction, this small capacity shift is likely reversible, caused by Li re-distribution to/from the excess anode overhang^{19,51,52} and/or partially isolated cathode particles. Quickly passivating side reactions could also cause small shifts in capacity at break-in, albeit irreversibly.

For the cycle-aged cells, the diffusion-induced-stress increase in C/3 li inventory is captured by $b_{3,N}$ in Table VII. It shares a similar functional form to $(b_{1,N})_D$ in Table V. We attribute this apparent Li gain to relaxation of transport losses in the positive due to reduction of positive particle solid-diffusion transport length with cycling. Apparently, the particles remain electrically connected to the electrode as they pulverize. The outcome is a reduction in effective particle size, shortening the NMC active material diffusion length which increases Li-ion availability for capacity measured at the C/3 rate.

To finalize the capacity fade model, we make slight improvements to the $b_{1,t}$ rate model (Fig. 8), including both calendar- and cycle-aging datasets. Adding cycle-aging datasets improves the calendar-fade model by introducing additional values of average SOC. SOC trends are more consistent across the tested temperatures. With all model equations identified, the improved calendar-fade sub-model yields global model (F) in Table V. Figure 9 plots the global model along with all test data. Residuals are nearly flat, indicating reasonable extrapolation into the future. Quality of fit is $R^2 = 0.990$, with an RMSE of 0.52% of capacity.

Complex cycling validation.—Two cells aged under an EV drive cycle— withheld from the fitting process—are used to validate the model for complex cycling. Unlike CC discharge cycles used for model fitting, 3 repetitions of the WLTP EV drive cycle (Fig. 10a) discharge the cell. CCCV charging is at the C/3 rate. To convert the model to handle complex cycles, time-based model states $b_{1,t}$ and $b_{3,t}$ are normalized using Eq. 6. Cycling-based states $b_{1,N}$ and $b_{3,N}$ are normalized using $m = \infty$ in Eq. 7. The interpretation is that the Rainflow microcycle that creates the maximum damage represents the average damage rate for the entire composite WLTP cycle. The convolution Eq. C-3 from Appendix C provides time-series values for $C_{chg}^{0.5}DOD^{0.5}$ and DOD whose maximum values are identical to that from the Rainflow algorithm. The identical results eliminate the need for Rainflow cycle counting.

Applied to the complex WLTP cycle, the capacity fade model (Fig. 10b) overpredicts the capacity loss with 2% error after 180 d of testing. A second replicate cell showed similar results. Beyond 180 d, the 2% error stays approximately constant for the remaining 110 d of testing. Given that the error is a constant offset, the model might be improved by including discharge current as an additional damage factor in the $b_{3,N}$ model. Discharge current was not varied in the

Table V. SEI-growth-rate model identification using hierarchical local/rate/global model-fitting procedure.

	$b_{1,t}$ (day ^{-1/2})	$b_{1,N}$ (various units)	R ²	RMSE ^{a)}
A) Calendar fade rate	A) Local model ($DOD = 0, t > 100$ d): ^{b)} $q = 1 - b_{1,t} t^{1/2} - b_3$ ($b_{1,t}$) _A = $Arr_{36k}(-0.082 + 2.81soc - 5.15soc^2 + 2.77soc^3)$		0.950	4.76e-4 day ^{-1/2}
B) Cycling damage rate, multiplicative with time	B) Local model ($DOD > 0, t > 100$ d): ^{c)} $q = 1 - (b_{1,t})_A b_{1,N} t^{1/2} - b_3$	($b_{1,N}$) _B = $\max[0, 6.44 Arr_{-42k} \times DOD^{0.5} C_{chg}^{0.5}(1 + 2.02soc) + 0.33] + 7.7 Arr_{-53} DOD^{7.2}$	0.997	0.311
C) Cycling damage rate, additive with time, $\sim N$	C) Local model ($DOD > 0, t > 100$ d): ^{d)} $q = 1 - (b_{1,t})_A t^{1/2} - (b_{1,t})_A b_{1,N} N^{1/2} - b_3$	($b_{1,N}$) _C = $\max[0, 2.74 Arr_{-46k} \times DOD^{0.5} C_{chg}^{0.5}(1 + 1.63soc) - 0.263] + 5.15 Arr_{-57} DOD^{6.3}$	0.998	0.166 (cycle/day) ^{-1/2}
D) Cycling damage rate, additive with time, $\sim N_{100}$	D) Local model ($DOD > 0, t > 100$ d): ^{e)} $q = 1 - (b_{1,t})_A t^{1/2} - (b_{1,t})_A b_{1,N} N_{100}^{1/2} - b_3$	($b_{1,N}$) _D = $\max[0, 3.24 Arr_{-58k} \times DOD^{0.5} C_{chg}^{0.5}(1 + 2.10soc) - 0.099] + 1.44 Arr_{-13} DOD^{6.0}$	0.999	0.00604 (equivalent full cycle/day) ^{-1/2}
F) Calendar fade rate	F) Global model ($T < 60$ °C): ^{f)} $q = 1 - b_{1,t} [t^{1/2} + 0.985 (b_{1,N})_D N_{100}^{1/2}] - (b_3)_E \left[1 - \exp\left(-\frac{t}{10}\right)\right]$ ($b_{1,t}$) _F = $Arr_{37k}(-0.000197 + 0.0101soc - 0.0157soc^2 + 0.00835soc^3 - 4.06 \times 10^{-6} soc T + 3.32 \times 10^{-5} \max(0, T - 328.15))$		0.985	0.00604

a) Root-mean-square error. b) Fitting parameters: $b_{1,t}$ and b_3 . c) Fitting parameters: $b_{1,t}$ and b_3 . d) Fitting parameters: $b_{1,t}$ and b_3 . e) Fitting parameters: $b_{1,t}$ and b_3 . f) Fitting parameters: $m = 0.985$ as well as all individual parameters in the $b_{1,t}$ rate law.

Table VI. Cycling damage rate $b_{1,N}$ for 50% and 100% duty-cycle aging, where duty cycle is the ratio of cycling time to total calendar time. Unlike model (B), models (C) and (D) provide a consistent rate across the two duty cycle conditions, important to correctly extrapolate accelerated cycle aging to real-world scenarios with more rest time.

Cycling damage rate (45 °C, 80% DOD, 50% SOC, C/3 charge)	$b_{1,N}$ (various units)		
	100% duty cycle	50% duty cycle	Difference
B) Multiplicative with time: $b_{1,t} b_{1,N} t^{1/2}$	2.897	2.432	16%
C) Additive with time; proportional to partial cycles: $b_{1,t} t^{1/2} + b_{1,N} N^{1/2}$	0.7665	0.7620	0.58%
D) Additive with time; proportional to equivalent full cycles: $b_{1,t} t^{1/2} + b_{1,N} N_{100}^{1/2}$	0.8570	0.8520	0.58%

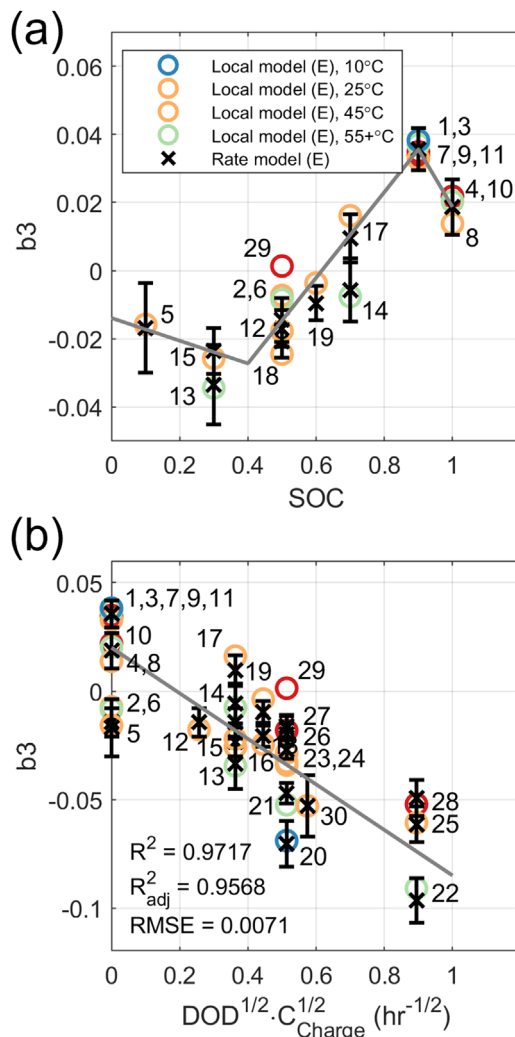
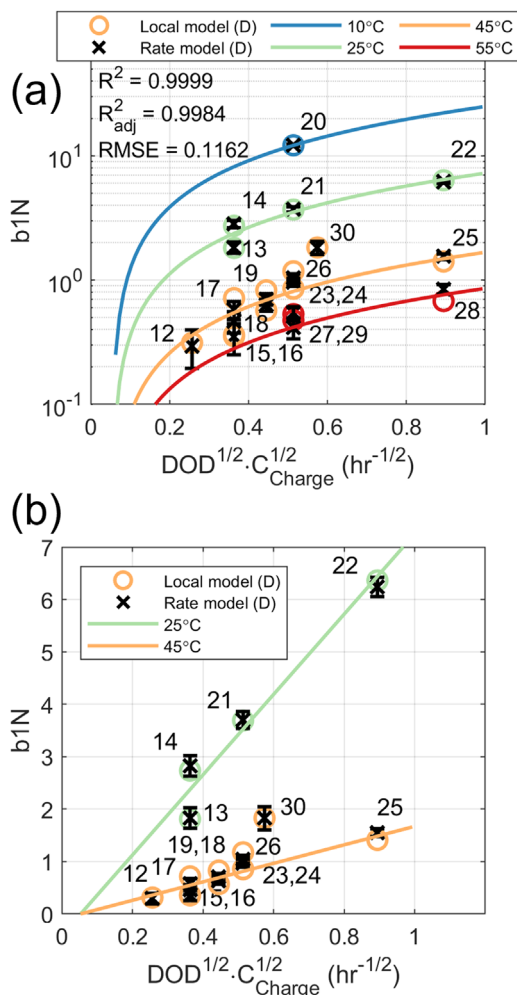


Figure 6. Rate model “(D)” in Table II describing cycling fade rate vs magnitude of concentration gradient, $DOD^{0.5}C_{chg}^{0.5}$. (a) All cycling conditions plotted on log scale. (b) Subset of cycling conditions plotted on linear scale. Trendlines are guide for the eye of diffusion-induced stress vs temperature.

aging design of experiments, though, so the impact of discharge current on the value of $b_{3,N}$ cannot be parameterized. Calendar fade SEI growth accounts for just 2% of the 10% fade observed over the 290 d test period. The cycling damage term, $q_{1,N} = b_{1,N}N_{100}^{1/2}$, accumulates 11% fade, an overprediction. The magnitudes of break-in terms, $b_{3,t}$ and $b_{3,N}$, are small, causing offsetting -1% and $+2\%$ shifts in initial capacity, respectively.

While model accuracy is reasonable, further research is warranted to identify how to reliably map constant-current test results to

Figure 7. Rate model “(E)” in Table VII showing Li loss (positive values) and gain (negative values) during break-in period. Data vs (a) SOC and (b) concentration gradient magnitude, $DOD^{0.5}C_{chg}^{0.5}$. Trendlines are guides for the eye to visualize (a) SOC-dependent calendar and (b) diffusion-induced stress-dependent cycling changes.

complex real-world-relevant usage. There are multiple ways to interpret a simple-cycling model and apply it to complex cycling. The present work does this by normalizing the cumulative damage of cycling-based terms (Eq. 7). With the convolution Eq. C.3 providing a time-series interpretation of cycling stress, it is also possible to recast the present model so that it can be continuously integrated with time. Similar to Delacourt (Eq. B-1), for example, the $q_{1,N} = b_{1,N}N_{100}^{1/2}$ state of the model would be calculated by integrating

Table VII. Lithium inventory break-in mechanism model identification with separate calendar- and cycling-dependent terms, respectively $b_{3,t}$ and $b_{3,N}$.

	$b_{3,t}$	$b_{3,N}$	R^2	RMSE
E) Local model ($t > 40$ d): ^{a)}	$q = 1 - (b_{1,t})_A [t^{1/2} - (b_{1,N})_D N_{100}^{1/2}] - b_3 b_3 = b_{3,t} + b_{3,N}$			
E) Rate	$(b_{3,t})_E = -0.0303 + 0.269 (1 - 1.360 soc) + 0.208 \max(0, soc - 0.3) - 0.272 \max(0, 0.9 - soc)$	$(b_{3,N})_E = \max[0, 0.0791 Arr_{-8.8k} \times DOD^{0.5} C_{chg}^{0.5} (1 + 1.143 soc) - 0.0386] + 0.178 \max(0, DOD - 0.85)$	0.971	0.0071

a) Fitting parameter: b_3 .

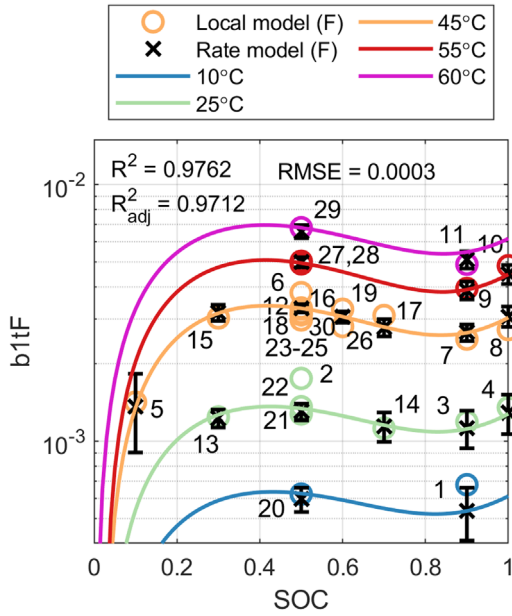


Figure 8. Rate model “(F)” in Table V for calendar fade including all data from both calendar- and cycle-aging tests.

the ODE

$$\frac{dq_{1,N}}{dt} = \frac{(b_{1,N}(T(t), SOC(t), I(t)))^2}{2} \frac{1}{q_{1,N}} \frac{1}{2 Ah_0} \frac{1}{3600 \frac{sec}{hr}} |I(t)|. \quad [12]$$

At that point the model would cease to be algebraic, however, and would require the use of ODE solvers to optimize the different model parameters embedded in ODEs, a logical next step. Additional future work is needed to improve methods that characterize the multitude of relevant degradation mechanisms and establish the most straightforward path to incorporate them into reduced- or full-order physics-based models.

Additional validation tests are needed to demonstrate model accuracy under path-dependent aging. Relevant real-world mixed-use cases might include slow charging interspersed with occasional fast charging, periods of storage at severe calendar aging (e.g. high temperature and SOC) followed by periods of realistic complex cycling (at normal temperature and SOC), and variable degradation with seasonal temperature changes.

Conclusions

This paper presents a framework to identify reduced-order algebraic life models from accelerated aging data. Mechanism and degradation rate/magnitude trial equations are selected based on

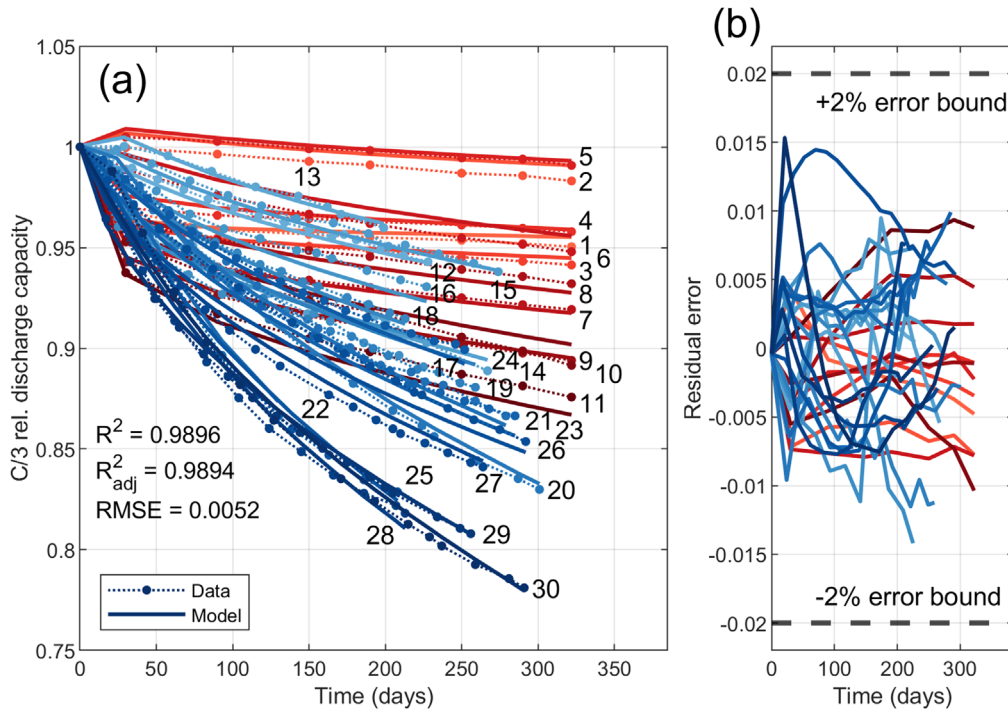


Figure 9. (a) Global model (F) in Tables II and III vs all data. (b) Model error vs training data.

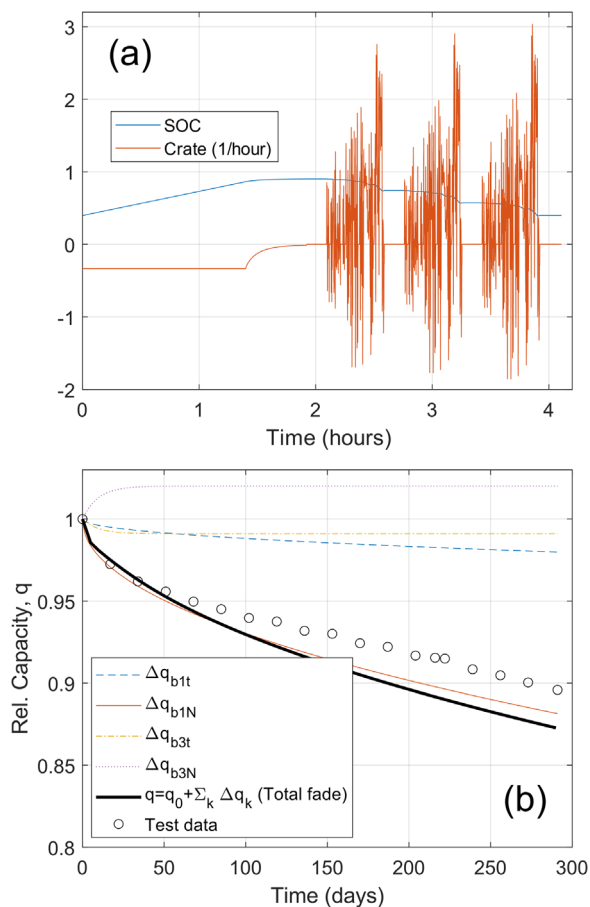


Figure 10. EV validation cycle. (a) SOC and current history for one cycle. (b) Model compared to observed capacity fade.

physical and statistical analysis of electrochemical data. The paper analyzes aging of a Li-ion graphite/NMC EV battery, uncovering well- and lesser-known capacity fade mechanisms. Incremental capacity analysis showed Li inventory loss controls capacity fade, with both side reactions and positive electrode loss contributing to Li inventory loss.

Analysis of the capacity fade data suggests dominant aging mechanisms:

1) Calendar fade tracks with square-root-of-time, due to diffusion-limited SEI growth:

- Temperature-dependence shows typical Arrhenius behavior.
- SOC-dependence is non-monotonic and does not follow typical Tafel behavior. Instead, the rate increases from 10% to 50%, decreases from 50% to 90% SOC, and then again increases from 90% to 100% SOC.
- Regarding the square-root-of-time dependence, if analyzing C/3 data only, one might conclude variable kinetic/diffusion limiting modes are present and vary the time exponent ($1/2$ for square root) across aging conditions as some authors choose. However, C/20 data on a log-log plot show quick convergence to the square-root trajectory, requiring just 100 d and 2% fade. In contrast, C/3 data require at least 200 d and 4% fade to converge. Since it is important to accurately deduce the long-term aging mode as quickly as possible, we recommend that low-rate capacity be measured at every capacity check. To keep test time short, this can be via a CV hold at end of C/3 discharge or a cascade discharge at progressively lower CC C-rates, ending around C/20.

2) Cycling fade tracks with square-root-of-cycling throughput due to an unknown mechanism:

- As this is the main degradation mechanism for the present cell, it is important to better understand in the future. Similar to calendar fade, C/20 cycling fade converges to the $1/2$ exponent twice as fast as C/3 data. For tracking cycling fade, full equivalent cycles, N_{100} , provides a more accurate model than the counting of partial cycles, N
- Given the $1/2$ exponent, this mechanism is likely coupled with SEI growth. As further support, the cycling fade-rate sub-model is more accurate when pre-multiplied by the SEI calendar-fade temperature- and SOC-dependent rate model. Plausible couplings with SEI growth are:

- Microcracking of the graphite negative and/or SEI layer with cycling
- Cathode cracking, surface area growth or surface reorganization that causes transition metal dissolution, its transport and deposition on the negative, where it catalyzes/accelerates SEI growth.

- Two factors capture aging-rate dependence, both suggesting electrode cracking is a root cause of accelerated cycling fade:

- Fade rate is nearly linear with $C_{chg} \sqrt{t_{chg}} = DOD^{0.5} C_{chg}^{0.5}$. This metric tracks active-material concentration-gradient magnitude, a proxy for diffusion-induced stress. Fade rate accelerates with low temperature.
- An extra term captures additional fade for 80% to 100% DOD cycling, likely linked to excessive resistance growth observed for 100% DOD cycling.

3) Calendar/cycling coupling:

- Incremental capacity analysis shows side reactions and positive electrode loss contribute to Li inventory loss in an additive manner.
- An additive model provided better quality of fit compared to a multiplicative calendar/cycling-coupled model. The multiplicative model had 16% fade-rate error on a 50% duty-cycle mixed-aging test case. The additive model had less than 1% error.

Lessor magnitude mechanisms include:

4) Break-in mechanisms cause initial shifts in measured capacity—either increasing or decreasing capacity—over the first 100 d.

- These mechanisms obscure the long-term fade-rate trajectory. They are important to understand if one hopes to develop an accurate life-predictive model from a brief aging test campaign.
- SOC dependence tracks non-monotonically similar to SEI growth: Initial capacity rises by several percent when the cell is stored from 10% to $\sim 40\%$ SOC, then begins to decrease from 40% to 90% SOC, but again increases from 90% to 100%. This behavior could be related to excess Li in anode overhang regions becoming accessible at certain SOC ranges or passivating side reactions at either electrode.
- Cycling dependence tracks similar to the electrode-cracking cycling-fade model, with magnitude nearly linear with $C_{chg} \sqrt{t_{chg}} = DOD^{0.5} C_{chg}^{0.5}$. Additional fade occurs at DODs greater than 80%.

To extend life predictions from simple (lab tests) to complex (real-world) cycling, fatigue models using number of cycles as an independent variable must resort to cycle counting or some current-integration assumption. Here, a convolution formula involving current/time superposition overcomes limitations with the Rainflow

cycle-counting algorithm and calculates a cumulative time-series signal that is a proxy for diffusion-induced stress. Previous work¹⁵ tracked a linear cycling fade mechanism whose rate was dependent on C_{rate} and $\sqrt{C_{rate}}$; The present work provides evidence for a square-root-of-cycling fade mechanism whose rate depends on $C_{rate} \sqrt{t_{pulse}} = C_{rate}^{1/2} DOD^{1/2}$.

The pathway beyond empirical cycling-fade correlations is to pursue a physics-based model approach that calculates transport, concentration-gradient-induced stress, and tracks damage accumulated based on that stress history. Several authors already use their mechanics models to calculate stress, but, to our knowledge, none has yet coupled stress to fatigue-driven damage accumulation. The recent review by Howey⁸ suggests that minimal additional work is required to couple stress with damage and capacity fade. The present analysis helps motivate additional mechanisms that must be included in physics-based models in order to predict lifetime. Future work is also needed to directly learn physical or empirical fade-rate equations for health-relevant parameters of an electrochemical model. Such a model could more widely describe evolving capacity rate capability and resistance changes over lifetime.

Acknowledgments

The National Renewable Energy Laboratory is operated by Alliance for Sustainable Energy under Contract No. DE-AC36-08GO28308 for the U.S. Department of Energy. Idaho National Laboratory is operated by Battelle Energy Alliance under Contract No. DE-AC07-05ID14517 for the U.S. Department of Energy. The views expressed in the article do not necessarily represent the views of the DOE or the U.S. Government. The U.S. Government retains and the publisher, by accepting the article for publication, acknowledges that the U.S. Government retains a nonexclusive, paid-up, irrevocable, worldwide license to publish or reproduce the published form of this work, or allow others to do so, for U.S. Government purposes.

Appendix A. Numerical Integration

Numerical integration of mixed diffusion/kinetic-limited side reaction model in Table III

$$\dot{x}(t) = k p \left(\frac{k}{x} \right)^{\left(\frac{1-p}{p} \right)} \quad [A.1]$$

requires special consideration at $t^{[0]} = 0$ where initial condition $x^{[0]} = 0$ and Eq. A.1 is singular. To integrate from $t^{[0]} = 0$ to $t^{[1]}$, the analytical solution should be used,

$$x^{[1]} = k (t^{[1]})^p. \quad [A.2]$$

Numerical integration of break-in process model in Table III

$$\dot{x}(t) = k (\max[0, M - x(t)]) \quad [A.3]$$

requires special consideration when the model is integrated across time periods with rising and falling levels of maximum damage, M . Care must be taken to ensure damage is irreversible. Equation A.3 partly takes care of this, ensuring rate of fade $\dot{x}(t) \geq 0$, ensuring damage is irreversible. When integrating (A.3) from timestep $t^{[i-1]}$ to $t^{[i]}$ however, one also needs to ensure the result $x^{[i]}$ does not step beyond the maximum permissible level of damage, $\max[M, x^{[i-1]}]$. To accomplish this, first calculate a temporary result $x^{[i]*} = x(t^{[i]})$. In the case of explicit time integration, the temporary result is

$$x^{[i]*} = x^{[i-1]} + k^{[i]} (\max[0, M^{[i]} - x^{[i-1]}]) (\Delta t) \quad [A.4]$$

Then calculate the final result, $x^{[i]}$ by checking that the temporary result does not exceed the maximum permissible level of damage,

$$x^{[i]*} = \min[x^{[i]*}, \max[M, x^{[i-1]}]] \quad [A.5]$$

Appendix B. Cumulative Damage Accrued by Complex Cycling

Unlike physics models that integrate electrochemo/mechanical states with respect to time, most reduced-order life models track damage with number of charge/discharge cycles. Described in Section 3.3, cycle-varying states cannot be continuously integrated with time for complex cycling. Instead, the user must assume that cycles are accumulated proportional to instantaneous current or use a method for cycle counting, such as the Rainflow algorithm.

Current integration accumulates damage based on the integral of current, square-root-of-current, energy or similar. Delacourt,¹⁵ for example, proposed an empirical formula for rate of active material loss,

$$\frac{dLAM}{dt} = C_1(T)|I(t)| + C_2(T)\sqrt{|I(t)|}, \quad [B.1]$$

where $C_1(T)$ and $C_2(T)$ are fitted functions.

Current integration conveniently avoids the need to count individual microcycles. For this reason, many authors track full-equivalent cycles rather than individual partial cycles. Partial cycles, N , are transformed to equivalent full cycles using $N_{100} = DOD \cdot N$. Equivalent full cycles can be continuously calculated by integrating charge current, discharge current, or the average of both directions:

$$N_{100} = \frac{1}{Ah_0 \left(\frac{3600 \text{ sec}}{\text{hr}} \right)} \int I_{chg}(t) dt \quad [B.2]$$

$$= \frac{1}{Ah_0 \left(\frac{3600 \text{ sec}}{\text{hr}} \right)} \int I_{dis}(t) dt \quad [B.3]$$

$$= \frac{1}{2 Ah_0 \left(\frac{3600 \text{ sec}}{\text{hr}} \right)} \int |I(t)| dt. \quad [B.4]$$

*Rainflow cycle-counting*⁵⁸ is popular in the mechanical fatigue discipline to discretize large and small stress/strain cycles, count them, and calculate their cumulative damage. The Rainflow algorithm transforms time-varying $SOC(t)$ into discrete microcycles $DOD_i = \Delta SOC_i$ each counted as either a whole or half cycle, $N_i = 1.0$ or 0.5 , respectively.

Disadvantages of Rainflow cycle-counting are that damage cannot be calculated in real-time—the representative period of cycling history must first be stored and processed—and that it occasionally returns drastically different aging results for two slightly different cycling histories. For instance, the counting of a half cycle with very small DOD at the end of a time-step, accumulated over many time-steps, could lead to a much larger partial cycle count than a cell with almost identical charge throughput but a slightly different voltage response. This much larger partial cycle count would not accurately reflect the accumulation of diffusion-induced stresses.

Appendix C. Convolution Alternative to Rainflow

In practice, the Rainflow algorithm occasionally discretizes complex cycling history into microcycles that are not physically relevant to diffusion-induced stress, as noted prior. We seek an alternative method to calculate stress acceleration functions involving DOD and C-rate (e.g., Table IV, Eq. 3.1) from current time-series data, $I(t)$. DOD of a CC microcycle, i , can be expressed as the

product of C-rate, C_i , and pulse time, t_i , as

$$DOD_i = C_i t_i \quad [C-1]$$

which means that acceleration factors involving products of DOD and C-rate can be written in terms of current and pulse time,

$$C_i^m DOD_i^n = \left(\frac{I_i}{Ah_0} \right)^{m+n} t_i^n \quad [C-2]$$

valid for simple cycling. For complex cycling with a time-series of current I_i at timestep t_i , a time-superposition formula can be expressed as

$$C_i^m DOD_i^n = \sum_{j=1}^i \left(\frac{I_j - I_{j-1}}{Ah_0} \right)^{m+n} (t_i - t_{j-1})^n \quad [C-3]$$

Each change in current experiences its own exponential decay with respect to time raised to the fractional power n . This type of formula is used, for example, in oil field analysis to extend an analytical model for flow rate vs constant pressure to estimate flow rate for a complex pressure history.⁶³

ORCID

Kandler Smith  <https://orcid.org/0000-0001-7011-0377>

References

- X. Hu, X. Lin, and M. Pecht, "Battery lifetime prognostics." *Joule*, **4**, 310 (2019).
- P. Tagade, K. Hariharan, S. Ramachandran, A. Khandelwal, A. Naha, S. M. Kolaka, and S. H. Han, "Deep Gaussian process regression for lithium-ion battery health prognosis and degradation mode diagnosis." *J. Power Sources*, **445**, 227281 (2020).
- J. Yang, C. Du, W. Liu, T. Wang, L. Yan, Y. Gao, X. Cheng, P. Zuo, Y. Ma, G. Yin, and J. Xie, "State-of-health estimation for satellite batteries based on the actual operating parameters—Health indicator extraction from the discharge curves and state estimation." *Journal of Energy Storage*, **31**, 101490 (2020).
- J. Feng, P. Kvam, and Y. Tang, "Remaining useful lifetime prediction based on the damage-marker bivariate degradation model: a case study on lithium-ion batteries used in electric vehicles." *Eng. Fail. Anal.*, **70**, 323 (2016).
- K. Qian, B. Huang, A. Ran, Y.-B. He, B. Li, and F. Kang, "State-of-health (SOH) evaluation on lithium-ion battery by simulating the voltage relaxation curves." *Electrochim. Acta*, **20**, 183 (2019).
- D. Yang, X. Zhang, R. Pan, Y. Wang, and Z. Chen, "A novel Gaussian process regression model for state-of-health estimation of lithium-ion battery using charging curve." *J. Power Sources*, **384**, 387 (2018).
- Y. Zhang, Q. Tang, Y. Zhang, J. Wang, U. Simming, and A. A. Lee, "Identifying degradation patterns of lithium ion batteries from impedance spectroscopy using machine learning." *Nat. Commun.*, **11**, 1706 (2020).
- J. Reniers, G. Mulder, and D. Howey, "Review and performance comparison of mechanical-chemical degradation models for lithium-ion batteries." *J. Electrochem. Soc.*, **166**, A3189 (2019).
- H. J. Ploehn, P. Ramadass, and R. E. White, "Solvent diffusion model for aging of lithium-ion battery cells." *J. Electrochem. Soc.*, **151**, A456 (2004).
- A. Colclasure, K. Smith, and R. Kee, "Modeling detailed chemistry and transport for solid-electrolyte-interface (SEI) films in Li-ion batteries." *Electrochim. Acta*, **58**, 33 (2011).
- R. Deshpande, M. Verbrugge, Y.-T. Cheng, and J. L. P. Wang, "Battery cycle life prediction with coupled chemical degradation and fatigue mechanics." *J. Electrochem. Soc.*, **159**, A1730 (2012).
- P. Arora, R. White, and M. Doyle, "Capacity fade mechanisms and side reactions in lithium-ion batteries." *J. Electrochem. Soc.*, **145**, 3647 (1998).
- C. Delacourt, A. Kwong, X. Liu, R. Qiao, W. Yang, P. Lu, S. Harris, and V. Srinivasan, "Effect of manganese contamination on the solid-electrolyte-interphase properties in Li-ion batteries." *J. Electrochem. Soc.*, **160**, A1099 (2013).
- X.-G. Yang, Y. Leng, G. Zhang, S. Ge, and C.-Y. Wang, "Modeling of lithium plating induced aging of lithium-ion batteries: transition from linear to nonlinear aging." *J. Power Sources*, **360**, 28 (2017).
- C. Delacourt and M. Safari, "Life simulation of a graphite/LiFePO₄ cell under cycling and storage." *J. Electrochem. Soc.*, **159**, A1283 (2012).
- X. Jin, A. Vora, V. Hoshing, T. Saha, G. Shaver, R. W. O. Garcia, and S. Varigonda, "Physically-based reduced-order capacity loss model for graphite anodes in Li-ion battery cells." *J. Power Sources*, **342**, 750 (2017).
- P. Gasper, K. Gering, E. Dufek, and K. Smith, "Challenging practices of algebraic battery life models through statistical validation and model identification via machine-learning." *J. Electrochem. Soc.*, **168**, 020502 (2021).
- M. Schimpe, M. E. von Kuepach, M. Naumann, H. C. Hesse, K. Smith, and A. Jossen, "Comprehensive modeling of temperature-dependent degradation mechanisms in lithium iron phosphate batteries." *J. Electrochem. Soc.*, **165**, A181 (2018).
- M. Naumann, F. B. Spingler, and A. Jossen, "Analysis and modeling of cycle aging of a commercial LiFePO₄/graphite cell." *J. Power Sources*, **451**, 227666 (2020).
- K. Smith, A. Saxon, M. Keyser, B. Lundstrom, Z. Cao, and A. Roc, "Life prediction model for grid-connected Li-ion battery energy storage system." *Proceedings of the American Control Conference* 4062 (2017).
- M. Dubarry, M. Berecibar, A. Devie, D. Anseau, N. Omar, and I. Villareal, "State of health battery estimator enabling degradation diagnosis: Model and algorithm description." *J. Power Sources*, **360**, 59 (2017).
- M. Dubarry and D. Beck, "Big data training data for artificial intelligence-based Li-ion diagnosis and prognosis." *J. Power Sources*, **479**, 228806 (2020).
- P. M. Attia, W. C. Chueh, and S. J. Harris, "Revisiting the t0.5 dependence of SEI growth." *J. Electrochem. Soc.*, **167**, 090535 (2020).
- E. V. Thomas, I. Bloom, J. P. Christophersen, and V. S. Battaglia, "Rate-based degradation modeling of lithium-ion cells." *J. Power Sources*, **206**, 378 (2012).
- J. Schmitt, A. Maheshwari, M. Heck, S. Lux, and M. Vetter, "Impedance change and capacity fade of lithium nickel manganese cobalt oxide-based batteries during calendar aging." *J. Power Sources*, **353**, 183 (2017).
- J. Belt, V. Utgikar, and I. Bloom, "Calendar and PHEV cycle life aging of high-energy, lithium-ion cells containing blended spinel and layered-oxide cathodes." *J. Power Sources*, **196**, 10213 (2011).
- E. Redondo-Iglesias, P. Venet, and S. Pelissier, "Eyring acceleration model for predicting calendar ageing of lithium-ion batteries." *Journal of Energy Storage*, **13**, 176 (2017).
- M. Ecker, J. B. Gerschler, J. Vogel, S. Kabitz, F. Hust, P. Dechent, and D. U. Sauer, "Development of a lifetime prediction model for lithium-ion batteries based on extended accelerated aging test data." *J. Power Sources*, **215**, 248 (2012).
- S. K. Rahimian, M. M. Forouzan, S. Han, and Y. Tang, "A generalized physics-based calendar life model for Li-ion cells." *Electrochim. Acta*, **348**, 136343 (2020).
- A. Eddahech, O. Briat, and J.-M. Vinassa, "Strategy for lithium-ion battery performance improvement during power cycling." *IECON Proceedings* 6806 (2013).
- M. Broussely, S. Herreyre, P. Biensan, P. Kasztejna, K. Nechev, and R. J. Staniewicz, "Aging mechanism in Li ion cells and calendar life predictions." *J. Power Sources*, **97**, 13 (2001).
- E. Sarasketa-Zabala, E. Martinez-Laserna, M. Berecibar, I. Gandiaga, L. M. Rodriguez-Martinez, and I. Villareal, "Realistic lifetime prediction approach for Li-ion batteries." *Appl. Energy*, **162**, 839 (2016).
- S. Kabitz, J. B. Gerschler, M. Ecker, Y. Yurdagal, B. Emmermacher, D. Andre, T. Mitsch, and D. U. Sauer, "Cycle and calendar life study of a graphite/LiNi_{1/3}Mn_{1/3}Co_{1/3}O₂ Li-ion high energy system. Part a: full cell characterization." *J. Power Sources*, **239**, 572 (2013).
- T. Lu, Y. Luo, Y. Zhang, W. Luo, L. Yan, and J. Xie, "Degradation analysis of commercial lithium-ion battery in long-term storage." *J. Electrochem. Soc.*, **164**, A775 (2017).
- M. Petit, E. Prada, and V. Sauvant-Moynot, "Development of an empirical aging model for Li-ion batteries and application to assess the impact of Vehicle-to-Grid strategies on battery lifetime." *Appl. Energy*, **172**, 398 (2016).
- A. Cordoba-Arenas, S. Onori, Y. Guezennec, and G. Rizzoni, "Capacity and power fade cycle-life model for plug-in hybrid electric vehicle lithium-ion battery cells containing blended spinel and layered-oxide positive electrodes." *J. Power Sources*, **278**, 473 (2015).
- J. Schmalstieg, S. Kabitz, M. Ecker, and D. U. Sauer, "A holistic aging model for Li(NiMnCo)O₂ based 18650 lithium-ion batteries." *J. Power Sources*, **257**, 325 (2014).
- J. Wang, P. Liu, J. Hicks-Garner, E. Sherman, S. Soukiazian, M. Verbrugge, H. Tataria, J. Musser, and P. Finamore, "Cycle-life model for graphite-LiFePO₄ cells." *J. Power Sources*, **196**, 3942 (2011).
- G. Suri and S. Onori, "A control-oriented cycle-life model for hybrid electric vehicle lithium-ion batteries." *Energy*, **96**, 644 (2016).
- W. Diao, S. Saxena, and M. Pecht, "Accelerated cycle life testing and capacity degradation modeling of LiCoO₂-graphite cells." *J. Power Sources*, **435**, 226830 (2019).
- E. Sarasketa-Zabala, I. Gandiaga, E. Martinez-Laserna, L. M. Rodriguez-Martinez, and I. Villareal, "Cycle ageing analysis of a LiFePO₄/graphite cell with dynamic model validations: Towards realistic lifetime predictions." *J. Power Sources*, **275**, 573 (2015).
- G. Sun, T. Sui, B. Song, H. Zheng, L. Lu, and A. Korsunsky, "On the fragmentation of active material secondary particles in lithium ion battery cathodes induced by charge cycling." *Extreme Mechanics Letters*, **9**, 449 (2016).
- S. Li et al., "Mutual modulation between surface chemistry and bulk microstructure within secondary particles of nickel-rich layered oxides." *Nat. Commun.*, **11**, 4433 (2020).
- F. Lin, I. Markus, D. Nordlund, T.-C. Weng, M.-D. Asta, H. Xin, and M. Doeff, "Surface reconstruction and chemical evolution of stoichiometric layered cathode materials for lithium-ion batteries." *Nat. Commun.*, **3529**, 5 (2014).
- P. Yan, J. Zheng, M. Gu, J. Xiao, J.-G. Zhang, and C.-M. Wang, "Intragranular cracking as a critical barrier for high-voltage usage of layer-structured cathode for lithium-ion batteries." *Nat. Commun.*, **14101**, 8 (2017).
- Z. Jiang, J. Li, Y. Yang, L. Mu, C. Wei, X. Yu, P. Pianetta, K. Zhao, and P. L. F. L. Y. Cloetens, "Machine-learning-revealed statistics of the particle-carbon/binder detachment in lithium-ion battery cathodes." *Nat. Commun.*, **11**, 2310 (2020).
- C.-F. Chen, P. Barai, K. Smith, and P. Mukerjee, "Scaling relations for intercalation induced damage in electrodes." *Electrochim. Acta*, **204**, 31 (2016).
- R. Xu, L. Vasconcelos, and K. Zhao, "Computational analysis of chemo-mechanical behaviors of composite electrodes in Li-ion batteries." *J. Materials Research*, **31**, 2715 (2016).

49. K. A. Severson et al., "Data-driven prediction of battery cycle life before capacity degradation." *Nat. Energy*, **4**, 383 (2019).
50. R. Deshpande, P. Ridgway, Y. Fu, W. Zhang, J. Cai, and V. Battaglia, "The limited effect of VC in graphite/NMC Cells." *J. Electrochem. Soc.*, **162**, A330 (2014).
51. M. Lewerenz, P. Dechent, and D. U. Sauer, "Investigation of capacity recovery during rest period at different states-of-charge after cycle life test for prismatic Li (Ni_{1/3}Mn_{1/3}Co_{1/3})O₂-graphite cells." *Journal of Energy Storage*, **21**, 680 (2019).
52. F. B. Spingler, M. Naumann, and A. Jossen, "Capacity recovery effect in commercial LiFePO₄/graphite cells." *J. Electrochem. Soc.*, **167**, 040526 (2020).
53. S. Santhanagopalan, K. Smith, J. Neubauer, G.-H. Kim, A. Pesaran, and M. Keyser, *Design and Analysis of Large Lithium-Ion Battery Systems* (Artech House, Boston) (2015).
54. M. Miner, "Cumulative damage in fatigue." *J. Appl. Mech.*, **12**, 149 (1945).
55. K. Smith and C.-Y. Wang, "Solid-state diffusion limitations on pulse operation of a lithium ion cell for hybrid electric vehicles." *J. Power Sources*, **161**, 628 (2006).
56. C. W. Gear and G. Kevrekidis, "Projective methods for stiff differential equations: problems with gaps in their eigenvalue spectrum." *SIAM J. Sci. Comput.*, **24**, 1091 (2006).
57. T. F. Fuller, "Bridging long temporal scales: durability analysis of electrochemical systems." *ECS Meeting Abstracts*, **1363**, MA2018 (2018).
58. ASTM International, "Standard practices for cycle counting in fatigue analysis." *ASTM E*, **03.01**, 1049 (2005).
59. M.-T. Rodrigues, K. Kalaga, S. S. I. Trask, and D. Abraham, "Anode-dependent impedance rise in layered-oxide cathodes of lithium-ion cells." *Journal of Electrochemical Society*, **165**, A1697 (2018).
60. M. Naumann, M. Schimpe, P. Keil, H. Hesse, and A. Jossen, "Analysis and modeling of calendar aging of a commercial LiFePO₄/graphite cell." *J. Energy Storage*, **17**, 153 (2018).
61. R. Xu, "Theories and experiments on the electro-chemo-mechanics of battery materials." *PhD Dissertation*, Purdue University (2018).
62. S. Cui et al., "Optimized temperature effect of Li-ion diffusion with layer distance in Li(NixMnyCoz)O₂ cathode materials for high performance Li-ion battery." *Adv. Energy Mater.*, **6**, 1501309 (2015).
63. H. Cinco-Ley and F. Samaniego, "The use and misuse of the superposition time function in well test analysis." *SPE Annual Technical Conference and Exhibition*, San Antonio, Texas (1989).
64. C. R. Birkl, M. R. Roberts, E. McTurk, P. G. Bruce, and D. A. Howey, "Degradation diagnostics for lithium ion cells." *J. Power Sources*, **341**, 373 (2017).